Electrochemical analysis of $Co_3(PO_4)_2.4H_2O$/graphene foam composite for enhanced capacity and long cycle life hybrid asymmetric capacitors

Abdulmajid A. Mirghni, Damilola Momodu, Kabir O. Oyedotun, Julien K. Dangbegnon and Ncholu Manyala*

Department of Physics, Institute of Applied Materials, SARCHI Chair in Carbon Technology and Materials, University of Pretoria, Pretoria 0028, South Africa.

*Corresponding author's email: ncholu.manyala@up.ac.za, Tel.: + (27)12 420 3549;

Highlights

- $Co_3(PO_4)_2 \cdot 4H_2O$/GF composite was successfully synthesized using a hydrothermal method.
- Graphene foam considerably improved the conductivity of the pristine $Co_3(PO_4)_2 \cdot 4H_2O$.
- Composite material showed pseudocapacitive electrochemical signature with high specific capacity.
- $Co_3(PO_4)_2 \cdot 4H2O$/GF was used with carbonized Fe-cation on PANI for a hybrid device.
- Hybrid device showed good cycle life (99% specific capacity) retention after 10000 cycles.

ABSTRACT

In this paper, we explore the successful hydrothermal approach to make $Co_3(PO_4)_2.4H_2O$/GF micro-flakes composite material. The unique sheet-like structure of the graphene foam (GF) significantly improved the conductivity of the pristine Co-based material, which is a key limitation in supercapacitors application. The composite electrode material exhibited superior capacitive conduct in 6 M KOH aqueous electrolyte in a 3-electrode set-up as compared to the pristine cobalt phosphate material. The material was subsequently adopted as a cathode in an asymmetric cell configuration with carbonization of Fe cations adsorbed onto polyaniline (PANI) (C-Fe/PANI), as the anode. The $Co_3(PO_4)_2.4H_2O$/GF//C-FP hybrid device showed outstanding long life cycling stability of approximately 99% without degradation up to 10000 cycles. A specific energy density as high as 24 W h kg^{-1}, with a corresponding power density of 468W kg^{-1} was achieved for the device. The results demonstrated the efficient utilization of the faradic-type $Co_3(PO_4)_2.4H_2O$/GF composite along with a functionalized carbonaceous electric double layer (EDL)-type material to produce a hybrid device with promising features suitable for energy storage applications.

KEYWORDS: Graphene; cobalt phosphate; Iron-carbonized polyaniline; hybrid capacitors: energy storage

GRAPHICAL ABSTRACT

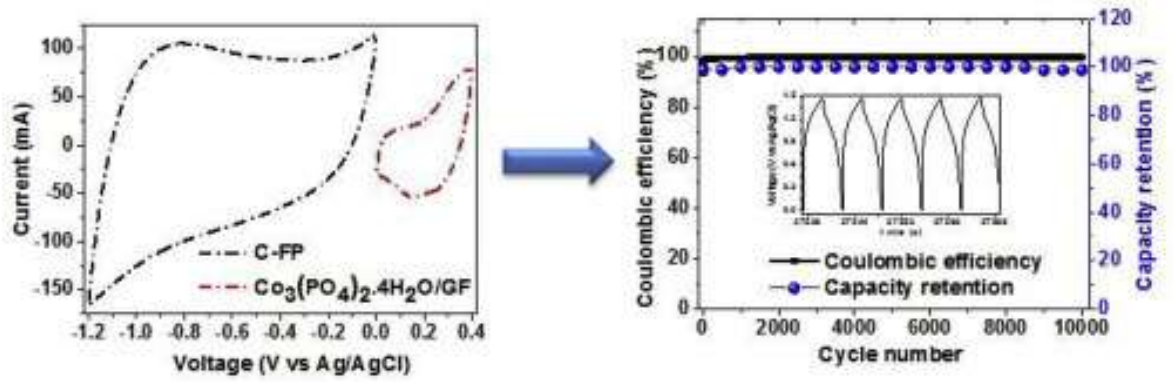

INTRODUCTION

Growing loads for convenient and flexible devices along with highly efficient electrical vehicles has promoted the fast growth of lightweight, extremely effective energy storage devices. Electrochemical capacitors also commonly stated as supercapacitors (SCs), because of their fast charge-discharge dynamics and respectable cyclic stability, have equally encouraged significant consideration. Based on their energy storage signature, supercapacitors are classified into two groups: (I) electrochemical double-layer (EDL) capacitors, and (II) redox capacitors.

Principally, energy storage from EDLCs rises actually due to the isolation of electronic and ionic charges at the boundary of the electrode materials and the electrolyte solution resulting in its electrostatic nature. Double-layers materials with a significant specific surface area (SSA), like carbon aerogels, activated carbon, graphene, carbon fibers, and carbon nanotubes are frequently used as electrode materials for this sort of capacitors. On the other hand, fast faradaic responses give raise to the materials at specific potentials as in batteries and take place in the redox capacitors. Currently, hybrid supercapacitors, which are an additive combination of benefits of both the electric double-layer capacitance and redox capacitance, have become a vital filed for electrochemistry researchers. Different oxide/hydroxide materials having variety in structures with a number of oxidation states (e.g. Ni, Ru, Mn, Co, Mo, etc.) and conducting polymers are used. Though, the expense factor and the significant electrical resistance of transition-metal oxides/hydroxides limits the device charge-discharge rate, energy density and power density when these materials are adopted as electrode materials. This limitation has inspired researchers into a further investigation into sourcing alternatively cheaper and more

conductive materials. Such alternative electrode materials are structured to have a combination of low cost accompanied by improved electrochemical performance.

Recently, in order to solve the limitation problems encountered in metal oxide/hydroxide based materials, graphene foam (GF) has been introduced as an outstanding candidate to increase the electrical conductivity of the electrode material. This because of the unique characteristic that GF exhibits such as high thermal conductivity, electrical conductivity, strength, specific surface and its intrinsic capacitance [1][2]. Tshifhiwa et al. [3] reported the effect of graphene foam (GF) on the electrochemical performance of CoAl-LDH after they used the hydrothermal approach to synthesise the pristine and the composite materials. The performance of the composites has improved as a result of an addition of the GF and showed 775.6 F g^{-1} at a specific current of 0.5 A g^{-1} in 6 M KOH aqueous electrolyte, while the pristine material showed 647.5 F g^{-1} at the same specific current and electrolyte [3]. These outcomes emphasized the significance of graphene as an ideal material for increasing the conductivity of the electrode materials.

Metal phosphates have been vastly and successfully adopted in catalysis applications [4][5][6] over the years and are only being tested recently for energy storage applications [7],[8],[9],[10],[11]. However, the promising trend recorded has inspired further research into their electrochemical energy storage capability. Specifically, cobalt phosphate has been adopted as favourable cathode materials for Li-ion battery materials [12], heterogeneous reagents [4], sorbents, ion exchangers [13], magnetic supplies [14] and supercapacitors [15] owing to the films of associated CoO_x and PO_4 polyhedra [16] which makes them suitable for these listed applications. Haiyan Li et al. [17] described the impact of the morphology Co-phosphate architecture for supercapacitor electrodes measured in three electrode setup and tested in a 3.0 M KOH aqueous solution. The device showed a specific capacitance of 350 F g^{-1} at 1 A g^{-1}, promising rate capability with a retained capacitance of up to 227 F g^{-1} at a 10 A g^{-1} specific current, and an improved cycling stability (102% after 1000 cycles). Huan Pang et al. [18] on the other hand synthesized cobalt phosphite microarchitectures composed of ultra-long nanoribbons using a hydrothermal technique. The material tested in a three-electrode measurements displayed a specific capacity of 312 F g^{-1} at 1.25 A g^{-1}, and excellent cycling characteristic whilst retaining up to 89.4% of its capacitance after 3000 cycles at 1.25 A g^{-1} in 3.0 M KOH. Yongfu Tang et al. reported mesoporous cobalt nickel phosphate as a novel material for supercapacitor. they used as-prepared cobalt nickel phosphate as positive and a home-made activated carbon as negative for asymmetric device. the device exhibited energy density of 45.8 W h kg^{-1} at the power density of 42.4 W kg^{-1}[19].Chongjun Zhao et al. studied

$Ni_3(PO_4)_2$/RGO/$Co_3(PO_4)_2$ (NRC) synthesized by hydrothermal loaded in situ on Co-foam. The device was assembled using NRC@Co foam as positive and Activated carbon as negative. The device achieved energy density of 44.82 W h kg^{-1} and power density of 428.6 W kg^{-1} at specific current of 0.12 A g^{-1}[20].

The incorporation of conductive agents such as graphene into $Co_3(PO_4)_2.4H_2O$ has been explored. As a result of the synergistic effect of graphene layers facilitate the dispersion of $Co_3(PO_4)_2.4H_2O$ microparticles and provide a large surface area which serves as an extensive transport platform for the electrolyte, avoid aggregation of the particles and enables a low diffusion resistance. The superior mechanical property of graphene sheets makes it being easily assembled into free-standing films of $Co_3(PO_4)_2.4H_2O$ particles. In spite of these progresses, there are very few reports in the literature including the preparation of $Co_3(PO_4)_2.4H_2O$ and synergizing with graphene foam (GF) to develop the electrode characteristics of the materials in a supercapacitor application. In most studies, Co-phosphate was primarily used as a catalyst in water oxidation application[21][22]. Hence, the addition of graphene into the active matrix of pristine $Co_3(PO_4)_2.4H_2O$ is considered as a novel way to improve its electrochemical performance as an electrode for supercapacitor applications.

Herein, we present the synthesis of $Co_3(PO_4)_2.4H_2O$ and $Co_3(PO_4)_2.4H_2O$/GF composite of flake-like morphology using a facile and environmentally friendly hydrothermal approach.

Our selection of the hydrothermal approach is due to the fact that it assists the construction of most complex materials with a preferred physio-chemical properties. It also offers significant merits like simplicity, cost effectiveness, high purity and crystallinity of synthesized materials, higher rate of reaction, flexibility in design of product morphologies, and lower temperature of operation in the presence of an appropriate solvent. The SEM images showed that the $Co_3(PO_4)_2.4H_2O$ was successfully coated by the sheet-like graphene foam (GF). This is because GF has a high conductivity and large surface area suitable for electrochemical surface reactions. Thus, the low conductivity of the active material can be easily overcome using GF. The $Co_3(PO_4)_2.4H_2O$/GF composite revealed a highest specific capacity of 40 mAh g^{-1} at a specific current of 0.5 A g^{-1} tested in 6 M KOH, while the pristine $Co_3(PO_4)_2.4H_2O$ shown a specific capacity of 29 mAh g^{-1} at a specific current of 0.5 A g^{-1}. An asymmetric supercapacitor ($Co_3(PO_4)_2.4H_2O$/GF//C-FP), fabricated using $Co_3(PO_4)_2.4H_2O$/GF as the cathode and carbonization of Fe cations adsorbed onto polyaniline (PANI) (C-Fe/PANI) anode exhibited a wide cell voltage of 1.5 V in 6 M KOH and an enhanced energy density of 24 Wh kg^{-1} at 0.5

A g^{-1} with matching power density of 469 W kg^{-1}. The device showed an exceptional cyclic stability with 99% capacity retained after 10.000 cycles at a specific current of 8.0 A g^{-1}.

2. EXPERIMENTAL DETAILS

2.1 Materials Synthesis

2.1.1. *Hydrothermal synthesis of pristine $Co_3(PO_4)_2.4H_2O$*

The experiment was held using analytical grade chemicals as acquired with no extra treatment. Initially, 45 mM of $CoN_2O_6.6H_2O$ (1.746 g) and 15 mM of $N_2H_9PO_4$ (0.264 g) precursors were used for the synthesis of cobalt phosphate by complete dissolution in separate 50 mL portions of deionized water, as demonstrated by Scheme 1. Then, the whole $CoN_2O_6.6H_2O$ solution was introduced slowly into the $N_2H_9PO_4$ solution and stirred for 3 h. The mixed product was transported into a closed, Teflon-lined, stainless-steel autoclave unit then saved at 200 °C heat for a period of 6 h before being permitted to naturally turn cold to the room temperature. The resultant precipitate was subsequently collected by filtration process and washed with deionized water a couple of times with final drying at 60 °C for 12 hours to get the $Co_3(PO_4)_2.4H_2O$ product and labelled as 1 in Scheme 1.

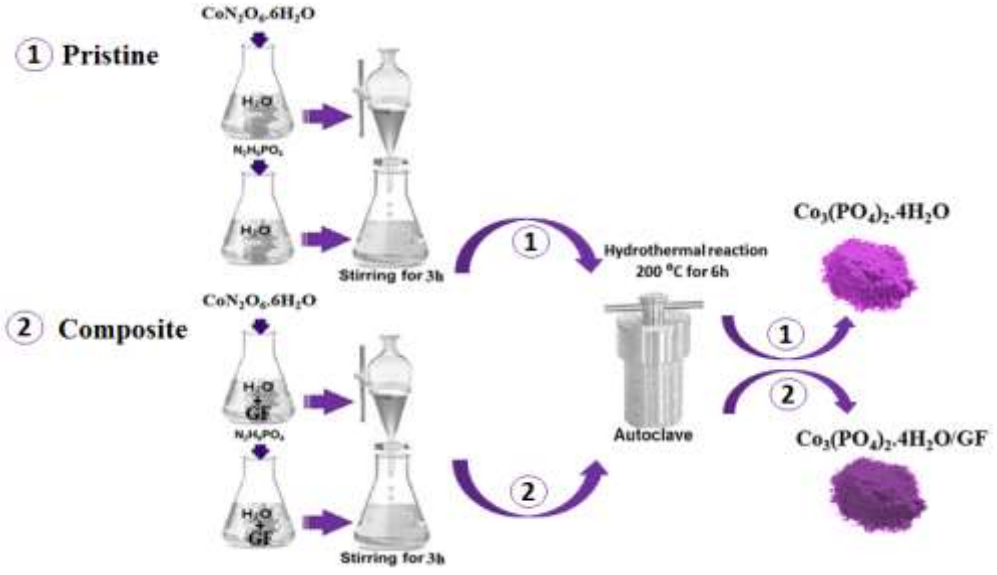

Scheme 1: Preparation steps of $Co_3(PO_4)_2.4H_2O$ and $Co_3(PO_4)_2.4H_2O$/GF

2.1.2. *Hydrothermal synthesis of $Co_3(PO_4)_2.4H_2O$/GF composites*

The graphene foam (GF) was prepared according to our recent work [23]. The $Co_3(PO_4)_2.4H_2O$/GF composite was prepared using a hydrothermal approach following the same procedure as shown in scheme 1 for the synthesis of the pristine material. Typically, an optimized mass of GF (60 mg) was dispersed in 50 mL of deionized water by ultra-sonication for 18 h at room temperature. Thereafter, 1.746 g of $CoN_2O_6.6H_2O$ and 0.264 g of $N_2H_9PO_4$ were added to a 50 mL portion of the sonicated GF solution and the full blend was further stirred for 3 h. The blend was further transmitted into an autoclave and kept at the same temperature and time as the pristine sample in section 2.1.1. The final $Co_3(PO_4)_2.4H_2O$/GF composite was cleaned a couple of times and dried for 12 h at 60 °C after the autoclave unit had cooled down and labelled as 2 in the Scheme 1.

2.1.3. *Synthesis of (C-Fe/PANI)*

Polyaniline, PANI was made following a simple polymerization procedure in which 1.0 M of aniline was liquefied in 1 M HCl to form the aniline hydrochloride salt. Afterward, 0.2 M of aniline hydrochloride (2.59 g aniline hydrochloride in 50 ml deionized water) was added to 0.25 M of ammonium peroxidisulfate (5.71 g of ammonium peroxidisulfate dissolved in 50 ml deionized water) and mixed overnight. The polymer precipitated as small particles then washed using water and acetone to eliminate excess HCl and catalyst. The negative electrode material; carbonization of Fe cations adsorbed onto polyaniline (PANI) (C-Fe/PANI), was synthesized as reported in our recent published work [24].

2.2 Materials analysis

The crystal investigation of the materials was studied using X-ray diffraction (XRD). An XPERT-PRO diffractometer (PANalytical BV, Netherlands) with theta/theta geometry, operating a cobalt tube at 35 kV and 50 mA, was used in this regard. The XRD patterns of all samples were verified in the range $7 - 45^0$ 2θ calculating every 5.240 seconds per step. A WITec Confocal Raman Microscope (WITec alpha300 R, Ulm, Germany).with a 523 nm laser wavelength, 4 mW laser power and 120-seconds spectral acquisition time was used to analyze the pristine $Co_3(PO_4)_2.4H_2O$ and $Co_3(PO_4)_2.4H_2O$/GF composites. The morphology of the product was further confirmed by a Zeiss Ultra Plus 55 field emission scanning electron microscope (FE-SEM) run at an increased voltage of 2.0 kV. Transmission electron

microscopy (TEM) analysis was made at 200 kV on a JEOL JEM-2100F microscope with field-emission gun. Typically, the samples sonicated for 30 minutes in an ethanol then the uniform dispersion dropped into the copper grid for analysis.

2.3 Electrochemical characterization

The electrochemistry analysis was done on a Bio-Logic multichannel setup (VMP300) potentiostat/galvanostatic at room temperature. Each electrode material was made such that the ratio of the active material, carbon black and the PVDF binder ruled by 8:1:1 and pasted on a nickel foam as a current collector while NMP was used as a solvent. The electrodes kept in an air oven overnight and the oven set at 60 ^{0}C to evaporate the NMP from the samples. The electrode materials were weighted to have an average mass loading of 2.6 mg each. The three electrode configuration was considered to study the electrochemistry of material using glassy carbon as a counter electrode and Ag/AgCl (3 M KCl saturated) as the reference electrode in 6 M KOH aqueous electrolyte with operating voltage-range between 0-0.4V. Asymmetric setup with different cathodic and anodic electrodes was accumulated such that two electrodes were isolated by microfiber glass filter paper in CR2025-type coin cells. The cyclic voltammetry and galvanostatic charge-discharge measurement of the devices were done in a voltage range from 0-1.5 V at different scan rates from 5 – 100 mV s^{-1} and specific current between 0.5–10 A g^{-1}. Electrochemical impedance spectroscopy (EIS) set-up was directed in a frequency range of 100 kHz to 0.01 Hz with an open circuit voltage using a sinusoidal signal of 5 mV. The charge and the specific capacity (C_s) of $Mn_3(PO_4)_2$/GF and C-FP could possibly be estimated from the CD curves according to the following formulas [25][26]:

$$Q(C.g^{-1}) = I_d \Delta t \quad \text{..... (1)}$$

$$C_s(\text{mAh g}^{-1}) = \frac{I_d \Delta t}{3.6} \quad \text{..... (2)}$$

where I_d is the specific current (A g^{-1}), , V is the potential window (V), m is the mass of the active electrode material (mg) and Δt is the discharge time (s).

In order to accumulate the hybrid device setup, the $Co_3(PO_4)_2.H_2O$/GF was used as the cathode and the C-FP as the anode. The quantity of charge, Q, deposited in each of the cathode and anode in a hybrid device must be equal and is ruled by Equations [26]:

$$Q_+ = Q_- \quad \text{..... (3)}$$

$$m_{+} I_{d(+)} \Delta t_{+} = m_{-} I_{d(-)} \Delta t_{-} \quad \text{(4)}$$

Where Q_{+} and Q_{-} denote the charges accumulated in both cathode and anode in that order.

Then it follows that the ratio of C-FP to $Co_3(PO_4)_2.4H_2O$/GF at the same specific current is:

$$\frac{m_{+}}{m_{-}} = \frac{233}{118} = 1.97 \quad \text{(5)}$$

Using Eq. (5), the final masses of the positive and negative electrodes were 3.8 mg and 2.0 mg respectively which implies that the total mass of the cell was 5.8 mg.

The energy density (E_d) and power density (P_d) of the cell were estimated considering the formulas below respectively [25]:

$$E_d (Wh.kg^{-1}) = \frac{i}{3.6(m_{+} + m_{-})} \int V dt \quad \text{(6)}$$

$$P_d (W.kg^{-1}) = 3600 \frac{E_d}{\Delta t} \quad \text{(7)}$$

Where $\int V dt$ represent the area under the discharge curve.

3. RESULTS ANALYSIS

Fig. 1(a) represents the X-ray diffraction of the pristine $Co_3(PO_4)_2.4H_2O$ sample and the corresponding Inorganic Crystal Structure Database ICSD-86668 (chemical formula: H_8 Co_3 O_{12} P_2; crystal system: orthorhombic; space-group: *Pcab (61)*; cell ratio a/b = 0.6448 b/c = 0.8456 c/a = 1.8339). The software Diamond - Crystal and Molecular Structure Visualization is used to analyze the structure of the $Co_3(PO_4)_2.4H_2O$ [27].

Fig. 1(b) shows the crystal structure of $Co_3(PO_4)_2.4H_2O$ viewed in the (210) plane using ICSD - 86668. In this structure, the Co-atoms are connected in an octahedral configuration giving rise to another Co-atom interconnected by phosphate (PO_4) groups. The configuration nearby the Co-atoms can be described as nearly ordered trigonal antiprism, which bases match to the faces joint with the neighbouring Co-atom. These form a lower electrostatic repulsion due to the +2 oxidation state of the cobalt [28][29]. Fig. 1(c) displays the X-ray diffraction design of the pristine $Co_3(PO_4)_2.4H_2O$ and the composite $Co_3(PO_4)_2.4H_2O$/GF.

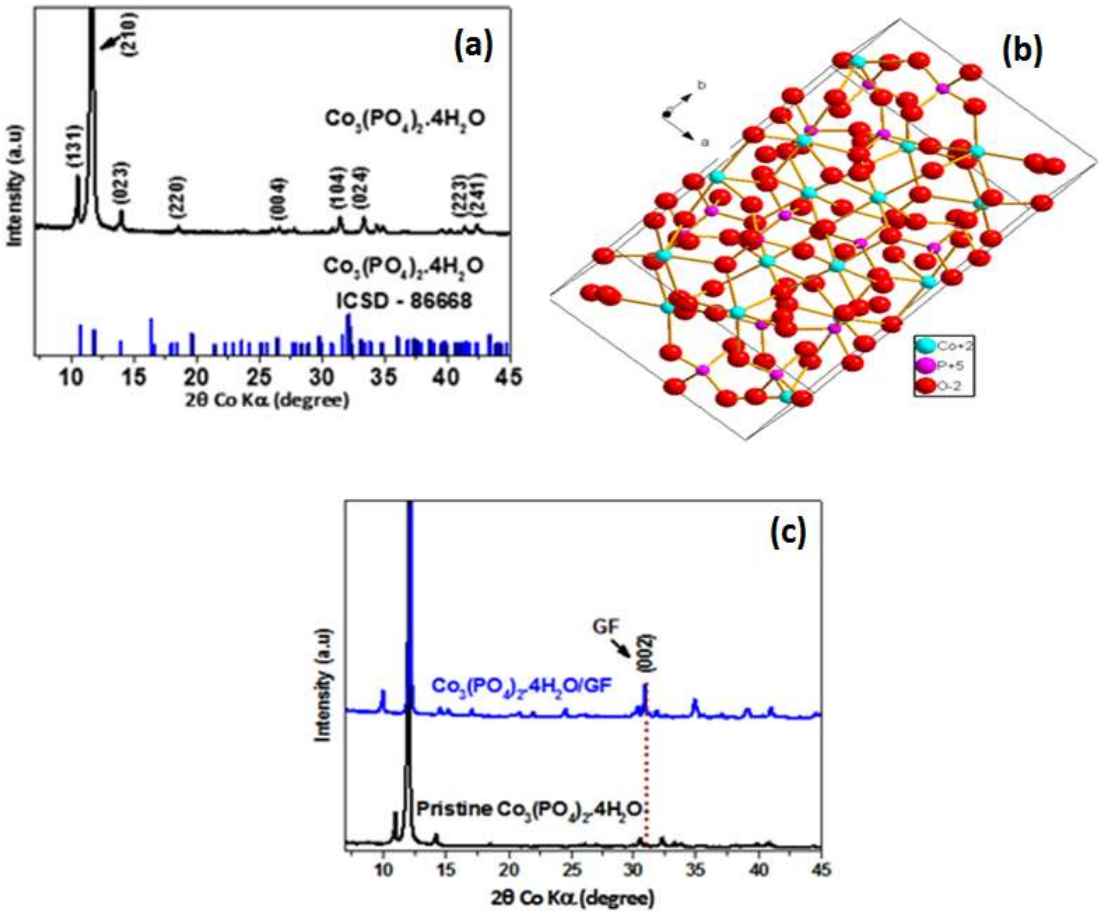

Fig. 1: (a) XRD pattern of the pristine $Co_3(PO_4)_2.4H_2O$ sample and the matching $Co_3(PO_4)_2.4H_2O$ ICSD card no. 86668 and (b) XRD pattern of the pristine $Co_3(PO_4)_2.4H_2O$ and $Co_3(PO_4)_2.4H_2O$/GF composite.

It is worth mentioning that the addition of graphene through the synthesis process supports the growth of $Co_3(PO_4)_2.4H_2O$ on the graphene sheets. Though, GF might influence the growth dynamics of the $Co_3(PO_4)_2.4H_2O$, it will not completely change the structure of the material, but could distort the original framework of the pristine $Co_3(PO_4)_2.4H_2O$ [30].

The Raman spectroscopy which demonstrates the interaction between the photon and the chemical bonds in the as-synthesized material is provided in Fig. 2. The pure graphene foam shows a typical Raman spectrum associated with graphene which illustrates the G-mode for carbon-carbon vibration mode at 1565 cm^{-1} and 2D-mode originating from the double resonance process at 2705 cm^{-1}. In the spectrum for the pure $Co_3(PO_4)_2.4H_2O$ sample, the peak at about ~948 cm^{-1} is assigned to the $Co_3(PO_4)_2.4H_2O$ vibrational stretching modes. In addition, the sharp Raman band at 948 cm^{-1} shows low-intensity features just below 948 cm^{-1} assigned to the $Co_3(PO_4)_2.4H_2O$ signatures [31]. The $Co_3(PO_4)_2.H_2O$/GF composite is composed of

characteristic peaks linked to the typical G- and 2D-band of graphene and $Co_3(PO_4)_2.4H_2O$ discussed earlier. However, a slight shift in the peaks is observed which is postulated to be due to the interaction of the graphene with Co-based pristine materials in the compound [32][33][34]. Besides, It can be seen that for the $Co_3(PO_4)_2.4H_2O$ /GF composite, the intensity is reduced considerably and that could be as a result of GF attached to the surface of the $Co_3(PO_4)_2.4H_2O$.

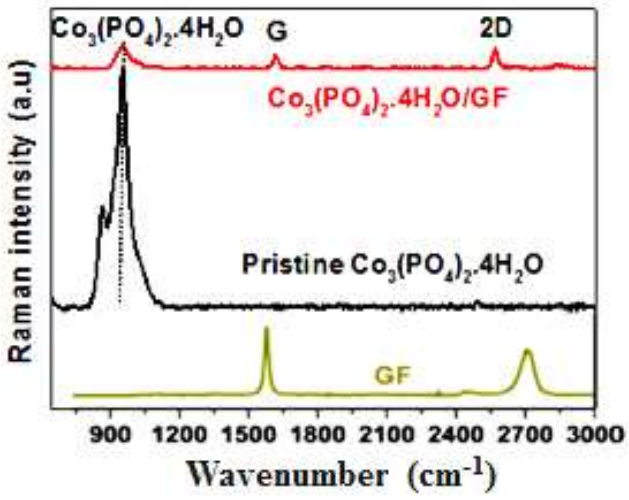

Fig. 2: The Raman spectra of the graphene foam (Gf), pristine $Co_3(PO_4)_2.4H_2O$ and $Co_3(PO_4)_2.4H_2O$/GF composites

Fig. 3(a-b) shows the morphological nature of the pristine Co-phosphate sample at low and high resolution in an order obtained from the SEM analysis. From this figure, the morphology of the $Co_3(PO_4)_2.4H_2O$ displays a sample composed of long hexagonal flakes.

Though, with the introduction of graphene foam into the active matrix, the $Co_3(PO_4)_2.4H_2O$ flakes are seen to effectively attach themselves to the sheet of graphene as shown in Fig. 3(c). A uniform dispersion of the $Co_3(PO_4)0_{20}.4H_2O$ flakes within the graphene sheet is observed which is vital for giving the essential surface required for effective electrochemical interactions.

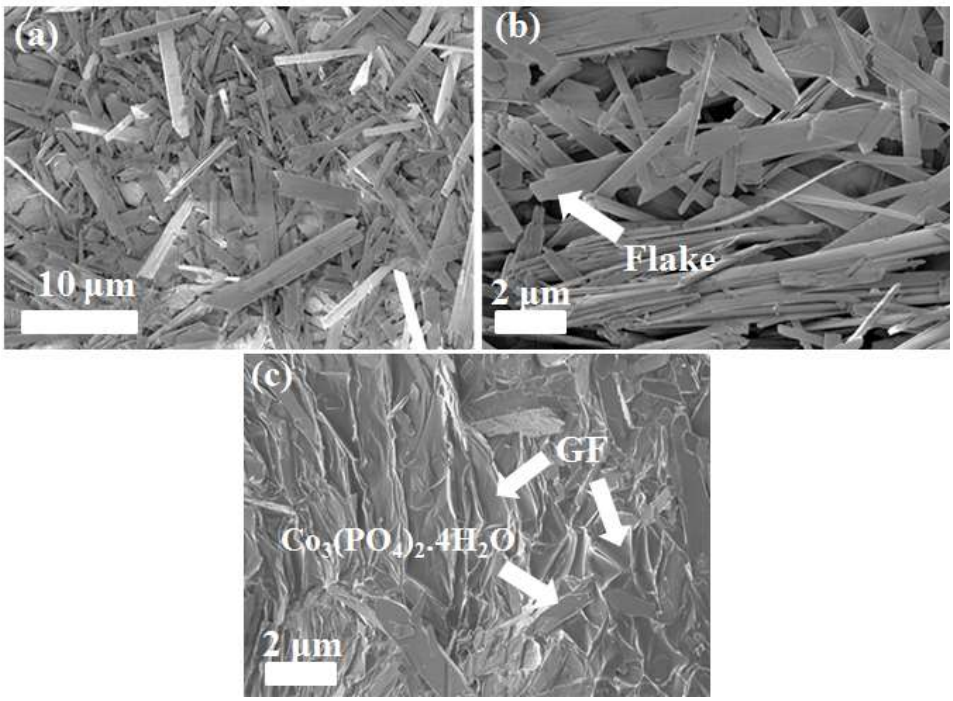

Fig. 3: SEM images of (a, b) pristine $Co_3(PO_4)_2.4H_2O$ sample at low and high magnification and (c) SEM image of composite $Co_3(PO_4)_2.4H_2O$/GF

The morphology of the pristine materials was further analysed using a transmission electron microscopy (TEM) technique and the results are clearly relayed in Fig. 4. The TEM micrographs confirmed the initial observations made from the SEM analysis. The TEM images of the pristine $Co_3(PO_4)_2.4H_2O$ sample shown in Fig. 4(a) also revealed the presence of micro-flakes with an average estimated thickness of less than 3 µm.

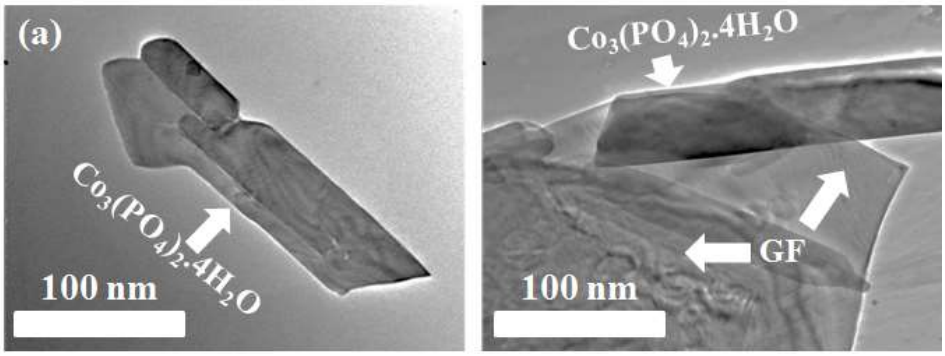

Fig. 4: TEM image of the (a) pristine $Co_3(PO_4)_2.4H_2O$ sample and (b) composite $Co_3(PO_4)_2.4H_2O$/GF

From the Fig. 4(b), it is clearly evident that the as-observed $Co_3(PO_4)_2.4H_2O$ micro-flakes are interconnected and uniformly covered by GF sheets to give rise to a good distribution of both materials within the composite.

To understand the electrochemical behaviour of the $Co_3(PO_4)_2.4H_2O$, cyclic voltammetry tests (CV) were initially performed to ascertain the ideal working potential for the as-prepared sample electrodes. Fig. 5(a) displays the CV curves of the $Co_3(PO_4)_2.4H_2O$ and $Co_3(PO_4)_2.4H_2O$/GF samples recorded at 100 mV s^{-1} within a 0.0 – 0.4 V vs Ag/AgCl potential window range. The CV curves did not exhibit any noticeable redox peaks and the shapes were quasi-rectangular indicating a possibility of containing possible EDLC and faradic attributes. For the fact that GF attaches to the surface of $Co_3(PO_4)_2.4H_2O$, the composite $Co_3(PO_4)_2.4H_2O$/GF has a better current response It can be seen that an addition of graphene foam (GF) to the pristine $Co_3(PO_4)_2.4H_2O$ material improves the current response of the $Co_3(PO_4)_2.4H_2O$/GF composite electrode material. This could be due to the synergistic interaction between the graphene sheets and $Co_3(PO_4)_2.4H_2O$ which increases the electrical conductivity of the composite material. [35]. Fig. 5(b) demonstrates the CD curve of $Co_3(PO_4)_2.4H_2O$ and $Co_3(PO_4)_2.4H_2O$/GF at a specific current of 0.5 A g^{-1}. These curves display the long discharge time of the $Co_3(PO_4)_2.4H_2O$/GF comparing to the $Co_3(PO_4)_2.4H_2O$ which are consistent with what CV curves are showing in Fig. 5(a).

Fig. 5(c) compares the specific capacity of the $Co_3(PO_4)_2.4H_2O$ and $Co_3(PO_4)_2.4H_2O$/GF composite for increasing specific current extending between 0.5 and 10.0 A g^{-1} calculated from the CD curves of which example of them is shown in in Fig. 5(b) for specific current of 0.5 Ag^{-1}.

The calculated specific capacity values for the pristine $Co_3(PO_4)_2.4H_2O$ were recorded between 22 – 29 mAh g^{-1} while the specific capacity values for $Co_3(PO_4)_2.4H_2O$/GF composite ranged between 23.0 – 39.8 mAh g^{-1} for the same specific current range. This confirms the observations from the CV and CD analysis in Fig. 5(a-b) with an improved current response for the $Co_3(PO_4)_2.4H_2O$/GF composite electrode showcasing a better performance based on its charge storage capability.

Fig. 5(d) displays the CV curves of the $Co_3(PO_4)_2.4H_2O$/GF composite at different scan rates from 5–100 mV s^{-1} in a potential window range of 0–0.4 V vs Ag/AgCl to ascertain the electrode stability with the increase in scan rate.

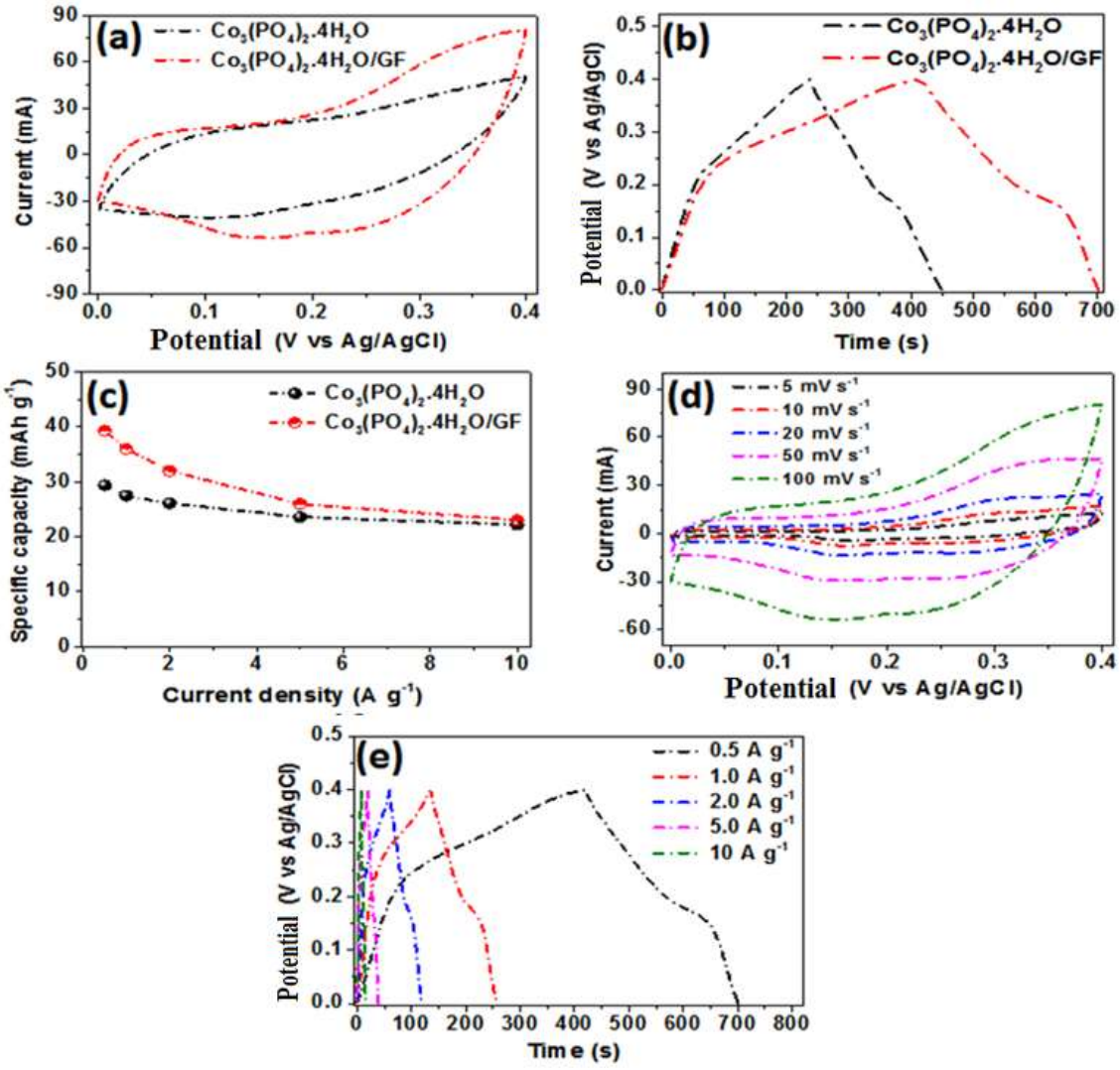

Fig. 5: (a) CV curves of pristine $Co_3(PO_4)_2.4H_2O$ and $Co_3(PO_4)_2.4H_2O$ /GF composites at scan rate of 100 mV s^{-1}, (b) CD curves of pristine $Co_3(PO_4)_2.4H_2O$ and $Co_3(PO_4)_2.4H_2O$ /GF composites at specific current of 0.5 A g^{-1} (c) specific capacity of pristine $Co_3(PO_4)_2.4H_2O$ and composites $Co_3(PO_4)_2.4H_2O$/GF calculated from the CD curves (d) CV curves of $Co_3(PO_4)_2.4H_2O$/GF composite within 5 – 100 mVs^{-1} (e) CD curves of $Co_3(PO_4)_2.4H_2O$/GF composite at different specific currents.

In this figure, it can be perceived that as scan rate rises the current response rises as result of a good reversibility of the electrode and also because of the constraint in the ion diffusion speed to gratify electronic deactivation of the redox response [36]. Fig. 5(d) shows the associated CD curves for the $Co_3(PO_4)_2.4H_2O$/GF composite electrode at specific current ranging from 0.5 to 10.0 A g^{-1} in a potential window range of 0.0 – 0.4 V vs Ag/AgCl. It is very evident that the CD curves are nonlinear in agreement with quasi-rectangular nature of the CV curves in Fig. 5(a) and confirms the claim of this material is indeed a combination of both EDLC and faradic charge storage behaviour.

Considering the good capacity of the $Co_3(PO_4)_2.4H_2O$/GF composite and the fast ion-transport property of the carbonized polyaniline grafted with Fe_3C (C-FP) material recorded from our earlier work [37], a hybrid device was assembled using these materials as the cathode and anode, respectively as shown in Fig. 6(a). For more evaluation of the electrochemical analysis and assess the individual steady potential windows of the $Co_3(PO_4)_2.4H_2O$/GF composite and C-FP sample electrodes, we also performed CV measurements in a three-electrode configuration for the C-FP material in 6 M KOH aqueous electrolyte solution before evaluating the electrochemical performance of the full asymmetric cell.

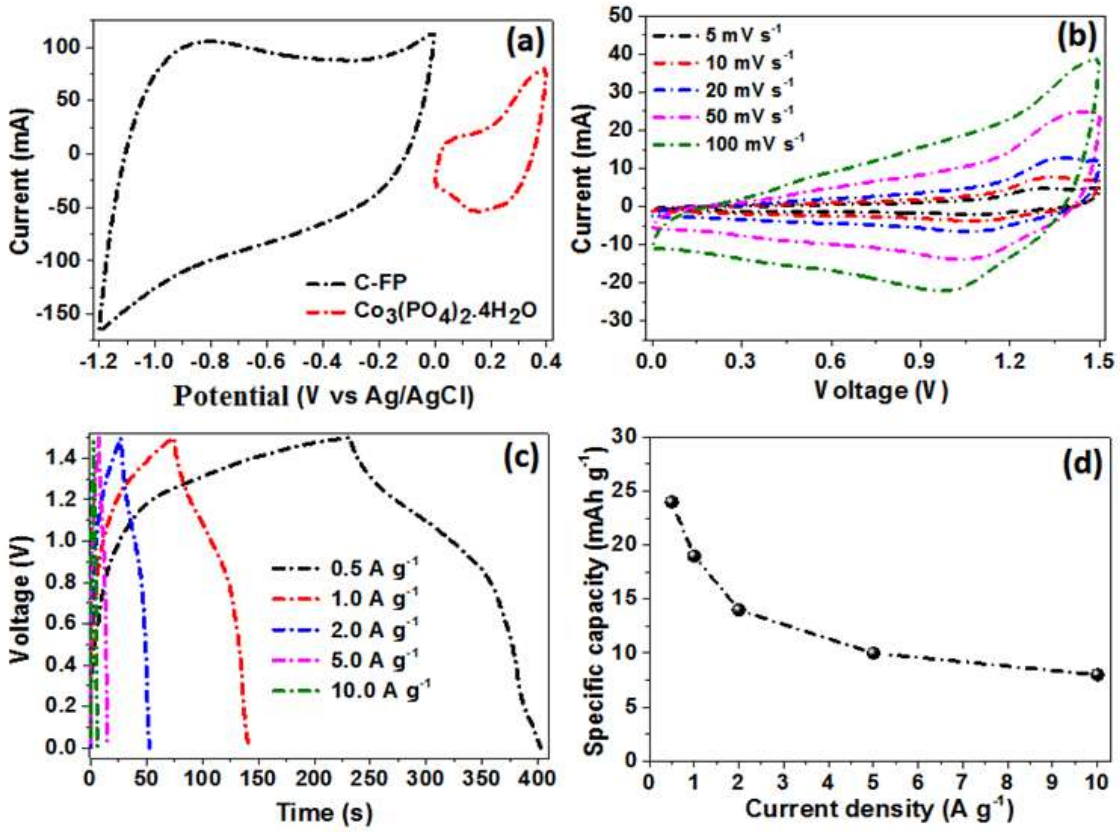

Fig. 6: (a) CV curves of the $Co_3(PO_4)_2.4H_2O$/GF and C-FP in three electrode measurement system at a 100 mV s^{-1}, (b) CV curves of the $Co_3(PO_4)_2.4H_2O$/GF//C-FP device within 5 – 100 mV s^{-1} at extended voltage of 0.0−1.5 V, (c) CD curves of the $Co_3(PO_4)_2.4H_2O$/GF//C-FP device at different specific currents in a voltage window range of 0.0−1.5 V and (d) specific capacity as a function of specific current for the $Co_3(PO_4)_2.4H_2O$/GF//C-FP device.

Fig. 6 (a) indicates that C-PF has a potential window of -1.2 – 0.0 V while that of $Co_3(PO_4)_2.4H_2O$/GF has a potential window of 0.0 – 0.4 vs Ag/AgCl at a scan rate of 100 mV s^{-1}. Both CV curves were relatively quasi-rectangular suggesting a good capacitive behavior for both samples. Built on the potential window of the $Co_3(PO_4)_2.4H_2O$/GF and C-FP

electrodes, the cell is expected to operate at a high cell voltage of 1.6 V, but was found to be stable for the voltage window of 1.5 V as presented in Fig. 6(b). This extended voltage could be due to the synergy of the individual material properties of the cathode and anode materials [38].

The galvanostatic charge-discharge curves of the $Co_3(PO_4)_2.4H_2O$/GF//C-FP asymmetric device were further tested under different specific currents as shown in Fig. 6(c) in the same cell voltage window. The specific capacities of the device obtained from the galvanostatic curves ranged from 8 − 24 mAh g^{-1} at specific currents ranging from 0.5−10 A g^{-1}. (see Fig. 6(d)). The specific capacity of the device decreases slightly as the specific current increases, due to the limited accessibility of the electrolyte ions at the high specific currents.

EIS measurements of the $Co_3(PO_4)_2.4H_2O$/GF//C-FP cell were further run at an open voltage and in a frequency range of 10 kHz – 100 mHz. At high frequency, the intercept on the *Z*'-axis signifies the Ohmic interior resistance indicated by R_S, which depicts the sum of intrinsic interface resistances of the working electrode material, the current collectors and electrolyte [39]. The shift from the high to mid-frequency area represented by R_{CT} expresses distance of the semicircle which is the amount of the charge transfer resistance. The charge transfer resistance R_{CT} expresses the interface resistance between the electrode and electrolyte. The Nyquist plot is shown in Fig. 7(a) represents the measured and fitting data (solid line) for the device and the corresponding circuit map revealed in Fig. 7(b). From the graph, the estimated values of R_s and R_{CT} are 0.26 Ohm and 0.5 Ohm respectively. The circuit in Fig. 7(b) was fitted from the EIS measured data using a software ZFIT/EC-Lab version 10.40. In this map, R_S is linked in a chain with the interface connection capacitance Q_{CT} and is in parallel with the charge transfer resistance R_{CT}. The deviation of the Nyquist plot from the ideal situation (ultimate polarizable capacitance that would give enlargement to a straight line parallel to the Z`` axis) in the high-frequency region proposes that a resistive constituent R_L is related with Q_L [40]. R_L is the leakage resistance which is placed in parallel with Q_L. The R_S and R_{CT} values and other parameters are in agreement with the measured data, showing an enhanced minimization of measured data within the cell with a negligible error value.

The device cycle life is also an important criterion for evaluating the electrochemical performance of a supercapacitor. In this regard, a constant galvanostatic charging−discharging test was conducted for 10 000 cycles at 8 A g^{-1} (Figure 7(c)). The inset to the figure shows a portion of charge-discharge curves for a few cycles' numbers.

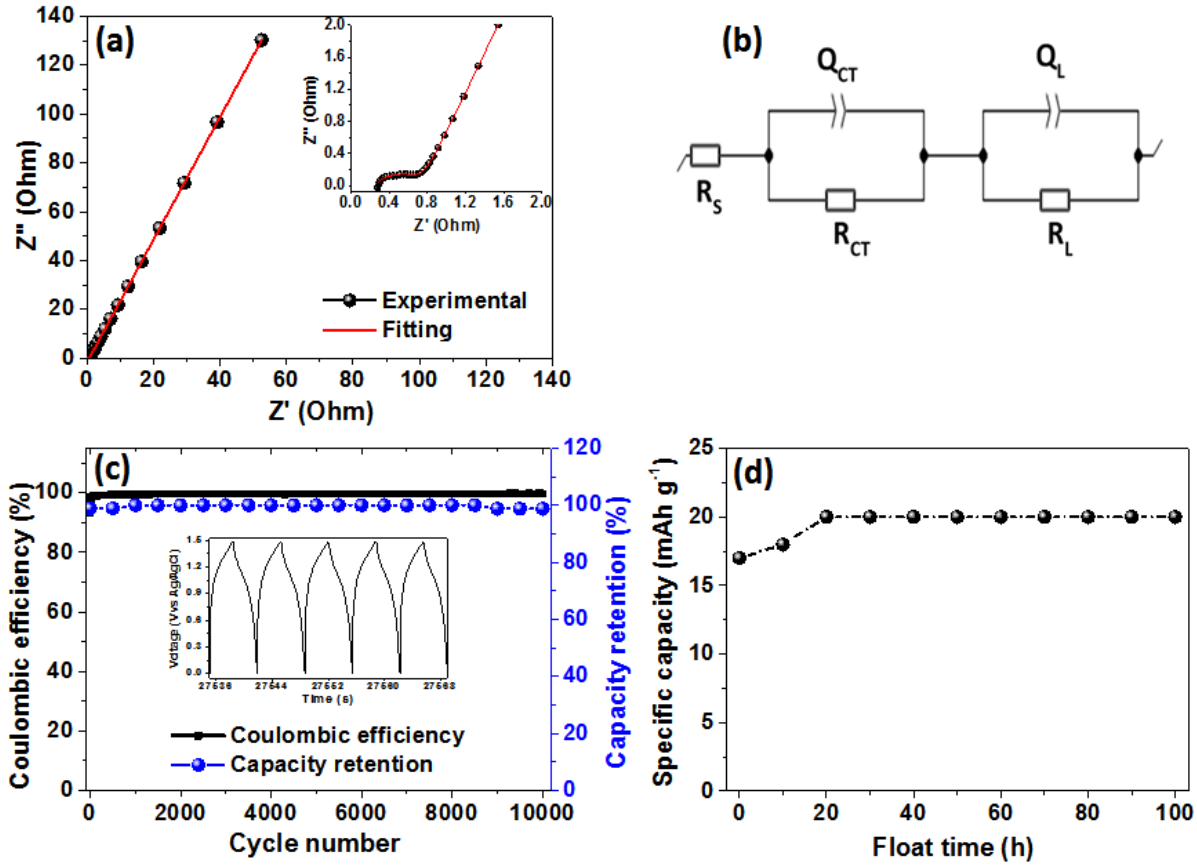

Fig. 7: (a) The Nyquist plot and (b) the corresponding diagram used to fit the EIS data in (a) as depicts by compacted line for $Co_3(PO_4)_2.4H_2O$/GF//C-FP device, (c) capacity retention and columbic efficiency versus cycle number for the $Co_3(PO_4)_2.4H_2O$/GF//C-FP device at a specific current of 8 A g^{-1} and (d) specific capacity versus float time.

Through the first 1000 cycles, the specific capacity amplified to some extent and this was linked to the re-activation of storage sites within the active material. The capacity retention was maintained at 99% for up to 10000 stability test cycles. Such excellent long-term cyclic stability might be ascribed to the subsequent two explanations: (i) The structured nature in the composite is favourable for the less diffusion of ions by resulting in low-resistance (in agreement with the R_s and R_{CT} values) pathways, and (ii) The graphene (GF) in the compounds enables the electrons transport through the charging and discharging mechanisms based on its superior electrical conductivity [41].

The device columbic efficiency was recorded at 100% depicting the perfectly reversible nature in the redox reaction taking place within the material. This indicates that repetitive cycling does not induce noticeable degradation in the electrode material's microstructure.

Floating performance has recently been reported to be a better means of studying device stability in which the device is held at a maximum operating voltage over several hours while monitoring its specific capacity [42] [43].

Fig. 7(d) shows the variance of the specific capacity with floating time for the $Co_3(PO_4)_2.4H_2O$/GF//C-FP asymmetric cell at a 5 A g^{-1} specific current. The asymmetric cell was subjected to a maximum operating voltage for 100 h with the specific capacity monitored after every 10 h period.

A gradual increase in values of specific capacity during the first 20 h was observed and this was thought to be mainly because of the fact that the ions need time before they completely penetrate in the electrode materials then stabilizing. Thereafter, the specific capacity values stabilized up to 100 h float time indicating well-stabilized electrode materials with no further capacity increase or decrease recorded. Peculiarly, the floating test over a significant number of cycling improved the electrochemistry properties of the material as result of complete penetration of the ions into the materials.

This was seen when a comparison of the specific capacity values of the device was made before and after subjecting to float tests. A higher device specific capacity value of 20 mAh g^{-1} was recorded as matched to the 10 mAh g^{-1} capacity recorded initially.

Fig. 8(a) represents the impedance exploration for the two electrode setup before stability, after stability and after float time tests. The R_S values estimated from the inset to the Fig. 8(a) are 0.26, 0.32 and 1.27 Ohm for the device before, after stability and after voltage holding respectively. It can be seen that there is an increase in R_s values but also there was also a corresponding improvement in electrochemical performance based on the ideal capacitance response recorded from the Nyquist plot which was more vertical to the imaginary impedance (Z") axis. Although the voltage holding process increased the cell resistance which is linked to more accessibility of ions in the electrode materials, an additional voltage holding step improved its ideal capacitive features [44]. This was also showed when a higher current response recorded from the CV analysis done after float time as shown in Fig. 8 (b).

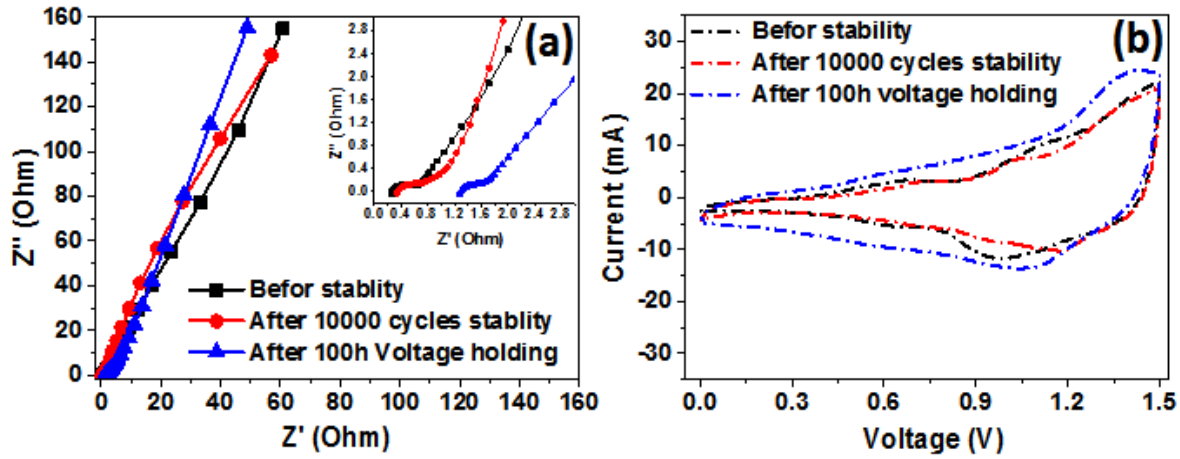

Fig. 8: EIS comparison of $Co_3(PO_4)_2.4H_2O$/GF//C-FP before, after stability and after voltage holding and (b) CV comparison of $Co_3(PO_4)_2.4H_2O$/GF//C-FP before , after stability and after voltage holding.

Fig. 9(a) displays a Ragone plot of the equivalent energy density *versus* power density values. The highest energy density of 24 Wh kg^{-1} with corresponding power density of 468 W kg^{-1} was recorded for the asymmetric device with an extended voltage of 1.5 V at specific current of 0.5 Ag^{-1}. These values are in the same order of magnitude and even higher as compared to similar phosphate-based asymmetric cells in the literature such as Co_2P//graphene (E_d = 24 Wh kg^{-1} and P_d = 300 W kg^{-1} @ specific current of 1 A g^{-1}) [45], $NH_4CoPO_4.H_2O$//graphene (E_d = 26.6 Wh kg^{-1} and P_d = 852 W kg^{-1} @ specific current of 1.5 A g^{-1}) [46], $Mn_3(PO_4)_2$//$Mn_3(PO_4)_2$ (E_d = 17.21 Wh kg^{-1} and P_d = 399.72 W kg^{-1} @ specific current of 0.5 A g^{-1}) and $Mn_3(PO_4)_2$//AC (E_d = 14.89 Wh kg^{-1} and P_d = 400.03 W kg^{-1} @ specific current of 0.5 A g^{-1}) [47]. , $Ni_3(PO_4)_2$/RGO/$Co_3(PO_4)_2$ (E_d = 44.82 Wh kg^{-1} and P_d = 428.6 W kg^{-1} @ specific current of 0.12 A g^{-1}) [20]. Moreover, the novelty of this work ley on stability. This could be seen when the device was subjected to a voltage holding in Figure 7(d) that the specific capacity remained stable for the period of 100 h, which shows no decreases in the specific capacity values rather increases in the first 30 h then stabilized throughout the aging time, signifying that the device exhibited excellent stability and no degradation.

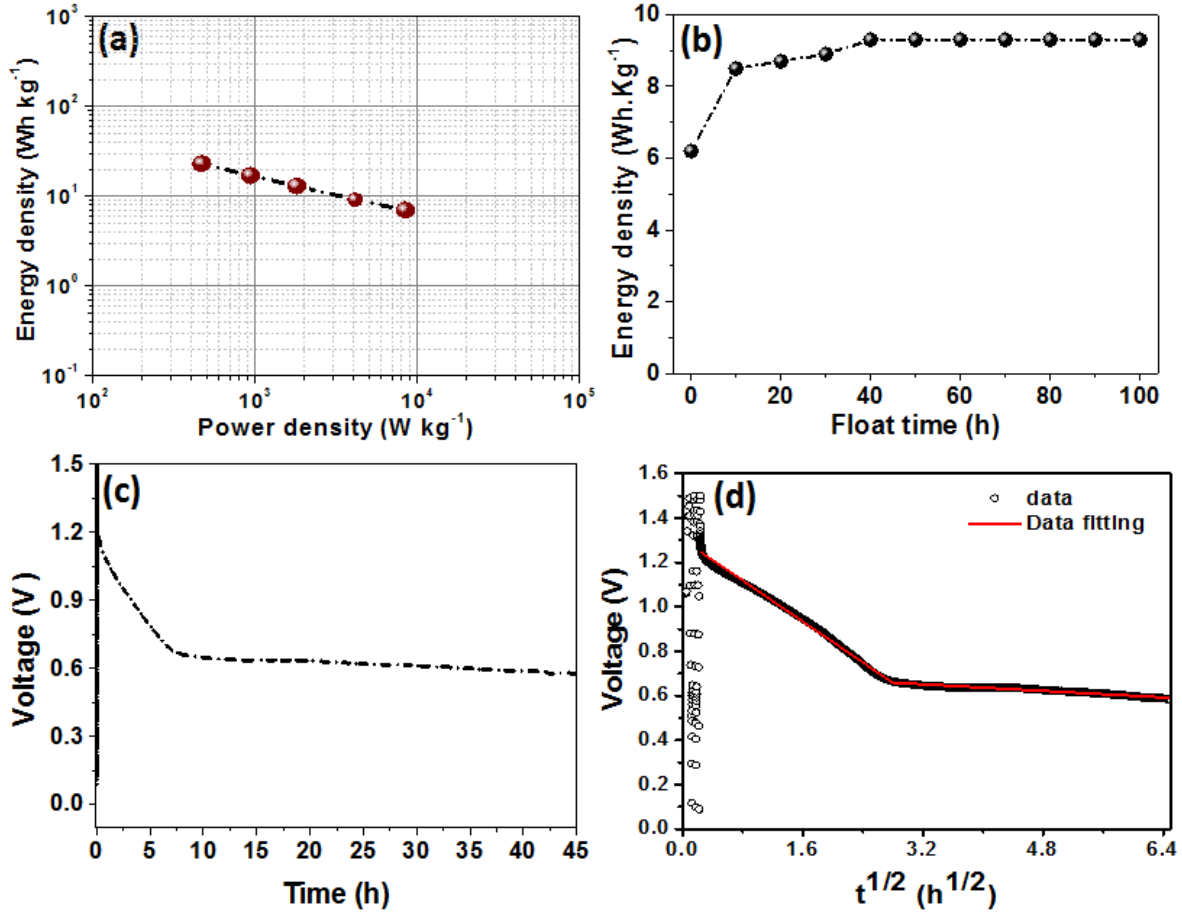

Fig. 9: (a) Ragone plot of $Co_3(PO_4)_2.4H_2O$/GF//C-FP device, (b) Energy density as a function of floating time for the $Co_3(PO_4)_2.4H_2O$/GF//C-FP device, (c) the self-discharge (SD) behaviour of the $Co_3(PO_4)_2.4H_2O$/GF//C-FP device and (d) associated self-discharge fitting data for the $Co_3(PO_4)_2.4H_2O$/GF//C-FP device

Based on the observed improvement in the device performance during cycling, the energy density was monitored after each 10 h voltage holding time (Fig. 9(b)) to further understand the effect on other cell parameters. Interestingly, the device energy density increases by 50% to finally stabilize after 30 h of float time at 9.3 Wh Kg^{-1}. This corresponds to the notable increase of 2.2% from the original value of 9.1 Wh Kg^{-1} recorded before at the same specific current of 10 Ag^{-1}. This improvement is due to the fact that pores had no full access to the ions with initial cycling. However, over time, dormant pores are activated which are accessible to the ions.

Furthermore, the nature of the self-discharge (SD) profile for the device was also investigated, as shown in Fig. 9(c). The device was charged to the highest possible voltage of 1.5 V and then set at an open circuit to observe the discharge profile over a period of 45 h.

It can be seen that there is a rapid drop in the device voltage at the first steps of the self-discharge over the first few hours which is probably due to the breakdown of water in the electrolyte. Thereafter, the voltage was seen to stabilize at a terminal voltage of 0.60 V for approximately 2 days. Furthermore, the data fits well with equation (1) which describe a diffusion controlled mechanism for the self-discharge observed (see Fig.9(d)) [48]:

$$V = V_o - mt^{0.5} \quad \text{(8)}$$

V is the instantaneous voltage recorded at any point in time *t*, given an initial voltage V_o and m is the diffusion parameter.

Explicitly using equation 8, the self-discharge data can be fitted with using equation 8 with two diffusion parameter m = 0.23 that used to fit the curve in range $0 – 2.8\ h^{1/2}$ and 0.01 that used to fit the curve in the range $2.8 – 6.5\ h^{1/2}$ for low and high holding time respectively. This diffusion-controlled mechanism may arise from the decomposition of the aqueous electrolyte which generates O_2 and H_2 species for water-based electrolyte.

4. CONCLUSION

This work introduces a hydrothermal approach synthesis of $Co_3(PO_4)_2.4H_2O$/GF. The material offers a decent mixture of cobalt phosphate and graphene foam, and demonstrates admirable pseudo-capacitive electrochemical behaviours and also indicating high specific capacity and an excellent cyclic stability. An assembled hybrid device built on the $Co_3(PO_4)_2.4H_2O$/GF as the cathode and carbonization of Fe cations adsorbed onto polyaniline (PANI) (C-Fe/PANI), as anode produced an energy density of 24 Wh kg^{-1} and a power density of 468 W kg^{-1} at a gravimetric specific current of 0.5 A g^{-1} . As much as the energy density of the asymmetric supercapacitor was seen to be similar and much better than other previous reports adopting similar materials, however the hybrid device demonstrates exceptional cycle life with 99% capacity retention after 10000 cycles and excellent stability demonstrated through voltage holding where 2.2% of specific capacity and hence the energy density was observed after 30h for high specific current of 10 A g^{-1}. The self-discharge profile was a purely diffusion controlled process with up to 0.60 V constituting its initial operating voltage still available after 45 h. Such material is expected to get a significant attention by the electrochemists as a candidate for application in high-performance energy storage systems.

ACKNOWLEDGEMENTS

This work is based on research supported by the South African Research Chairs Initiative (SARChI) of the Department of Science and Technology and the National Research Foundation (NRF) of South Africa (Grant No. 61056). Any opinion, finding and conclusion or recommendation expressed in this material is that of the author(s) and the NRF does not accept any liability in this regard. Abdulmajid A. Mirghni acknowledges the financial support from University of Pretoria, the NRF through the SARChI in Carbon Technology and Materials, and also Al Fashir University, Sudan.

REFERENCES

[1] C. Lee, X. Wei, J.W. Kysar, J. Hone, Measurement of the Elastic Properties and Intrinsic Strength of Monolayer Graphene, Sci. 321 (2008) 385-388.

[2] B.Z.J.Æ.A. Zhamu, Processing of nanographene platelets (NGPs) and NGP nanocomposites : a review, J. Mater. Sci. 43 (2008) 5092–5101.

[3] T.M. Masikhwa, M.J. Madito, A. Bello, J.K. Dangbegnon, N. Manyala, High performance asymmetric supercapacitor based on molybdenum disulphide/graphene foam and activated carbon from expanded graphite, J. Colloid Interface Sci. 488 (2017) 155–165.

[4] Y. Chang, N.E. Shi, S. Zhao, D. Xu, C. Liu, Y.J. Tang, Z. Dai, Y.Q. Lan, M. Han, J. Bao, Coralloid $Co_2P_2O_7$ Nanocrystals Encapsulated by Thin Carbon Shells for Enhanced Electrochemical Water Oxidation, ACS Appl. Mater. Interfaces. 8 (2016) 22534–22544.

[5] Z. Cai, W. Xu, F. Li, Q. Yao, X. Chen, Electropolymerization Fabrication of Co Phosphate Nanoparticles Encapsulated in N,P-Codoped Mesoporous Carbon Networks as a 3D Integrated Electrode for Full Water Splitting, ACS Sustain. Chem. Eng. 5 (2017) 571–579.

[6] T. Zhou, Y. Du, D. Wang, S. Yin, W. Tu, Z. Chen, A. Borgna, R. Xu, Phosphonate-Based Metal-Organic Framework Derived Co-P-C Hybrid as an Efficient Electrocatalyst for Oxygen Evolution Reaction, ACS Catal. 7 (2017) 6000–6007.

[7] X. Ma, W. Zhang, L. Kong, Y. Luo, L. Kang, RSC Advances Electrochemical

performance in alkaline and neutral electrolytes of a manganese phosphate material possessing a broad potential window, RSC Adv. 6 (2016) 40077–40085.

[8] S. Vadivel, D. Maruthamani, M. Kumaravel, B. Saravanakumar, B. Paul, S.S. Dhar, K. Saravanakumar, V. Muthuraj, Supercapacitors studies on $BiPO_4$ nanoparticles synthesized via a simple microwave approach, J. Taibah Univ. Sci. (2016) 2–7.

[9] X. Wang, Z. Yan, H. Pang, W. Wang, G. Li, Y. Ma, H. Zhang, X. Li, J. Chen, $NH_4CoPO_4.H_2O$ microflowers and porous $Co_2P_2O_7$ microflowers: Effective electrochemical supercapacitor behavior in different alkaline electrolytes, Int. J. Electrochem. Sci. 8 (2013) 3768–3785.

[10] K.H. Lee, Y. Lee, S.W. Lee, J.S. Ha, S. Lee, J.G. Son, Ice-templated Self-assembly of $VOPO_4$ – Graphene Nanocomposites for Vertically Porous 3D Supercapacitor Electrodes, Nat. Publ. Gr. 5 (2015) 1–10.

[11] B. Senthilkumar, Z. Khan, S. Park, K. Kim, H. Ko, Y. Kim, Highly porous graphitic carbon and $Ni_2P_2O_7$ for a high performance aqueous hybrid supercapacitor, J. Mater. Chem. A. 3 (2015) 21553–21561.

[12] G. Hautier, A. Jain, S.P. Ong, B. Kang, C. Moore, R. Doe, G. Ceder, Phosphates as lithium-ion battery cathodes: An evaluation based on high-throughput ab initio calculations, Chem. Mater. 23 (2011) 3495–3508.

[13] H.N.C.H. Nh, C. Po, J.R.D. Debord, R.C. Haushalter, J. Zubieta, The First Organically Templated Layered Cobalt Phosphates: Hydrothermal Syntheses and Crystal Structures of $[H_3N(CH_2)_3NH_3]_{0.5}[Co(PO_4)].\ _{0.5}H_2O$ and $[H_3N(CH_2)_4NH_3]_{0.5}[Co(PO_4)]$, J. Solid state Chem. 125 (1996) 270–273.

[14] P. Feng, X. Bu, G.D. Stucky, Synthesis and Characterizations of a Polymorphic Sodium Cobalt Phosphate with Edge-Sharing Co^{2+} Octahedral Chains, J. Solid State Chem. 131 (1997) 160–166.

[15] H. Pang, Z. Yan, W. Wang, J. Chen, J. Zhang, H. Zheng, Facile fabrication of $NH_4CoPO_4{\cdot}H_2O$ nano/microstructures and their primarily application as electrochemical supercapacitor, Nanoscale. 4 (2012) 5946–5953.

[16] G. Centi, Vanadyl Pyrophosphate - A Critical Overview, Catal. Today. 16 (1993) 5–26.

[17] H. Li, H. Yu, J. Zhai, L. Sun, H. Yang, S. Xie, Self-assembled 3D cobalt phosphate octahydrate architecture for supercapacitor electrodes, Mater. Lett. 152 (2015) 25–28.

[18] H. Pang, Y. Liu, J. Li, Y. Ma, G. Li, Y. Ai, J. Chen, J. Zhang, H. Zheng, Cobalt phosphite microarchitectures assembled by ultralong nanoribbons and their application as effective electrochemical capacitor electrode materials, Nanoscale. 5 (2013) 503–507.

[19] Y. Tang, Z. Liu , W. Guo, T. Chen, Y. Qiao, S. Mu, Y. Zhao, F. Gao, Honeycomb-like mesoporous cobalt nickel phosphate nanospheres as novel materials for high performance supercapacitor, Electrochim. Acta 190 (2016) 118–125.

[20] C. Zhao, S. Wang, Z. Zhu, P. Ju, C. Zhao, X. Qian, Roe-shaped $Ni_3(PO_4)_2$/RGO/$Co_3(PO_4)_2$ (NRC) nanocomposite grown in situ on Co foam for superior supercapacitors, J. Mater. Chem. A. 5 (2017) 18594–18602.

[21] D.K. Zhong, M. Cornuz, K. Sivula, M. Grätzel, D.R. Gamelin, Photo-assisted electrodeposition of cobalt–phosphate (Co–Pi) catalyst on hematite photoanodes for solar water oxidation, Energy Environ. Sci. 4 (2011) 1759–1764.

[22] M.W. Kanan, J. Yano, Y. Surendranath, M. Dincă, V.K. Yachandra, D.G. Nocera, Structure and Valency of a Cobalt−Phosphate Water Oxidation Catalyst Determined by in Situ X-ray Spectroscopy, J. Am. Chem. Soc. 132 (2010) 13692–13701.

[23] A.A. Mirghni, M.J. Madito, T.M. Masikhwa, K.O. Oyedotun, A. Bello, N. Manyala, Hydrothermal synthesis of manganese phosphate/graphene foam composite for electrochemical supercapacitor applications, J. Colloid Interface Sci. 494 (2017) 325–337.

[24] M.N. Rantho, M.J. Madito, N. Manyala, Symmetric supercapacitor with supercapattery behavior based on carbonized iron cations adsorbed onto polyaniline, Electrochim. Acta. 262 (2018) 82–96.

[25] L. Qian, L. Lu, Fabrication of three-dimensional porous graphene-manganese dioxide composites as electrode materials for supercapacitors, Colloids Surfaces A Physicochem. Eng. Asp. 465 (2015) 32–38.

[26] T. Nguyen, M. Boudard, M.J. Carmezim, M.F. Montemor, Layered Ni(OH)$_2$-$Co(OH)_2$ films prepared by electrodeposition as charge storage electrodes for hybrid

supercapacitors, Nat. Publ. Gr. (2017) 1–10.

[27] G. Bergerhoff, M. Berndt, K. Brandenburg, Evaluation of Crystallographic Data with the Program DIAMOND, J. Res Natl Inst Stand Technol. 101 (1996) 221–225.

[28] H. Effenberger, Structure refinement of $Co_3(OH)_2(PO_3OH)_2$ and $Co[PO_2(OH)_2]_2.2H_2O$, Acta Crystallogr. Sect. C Cryst. Struct. Commun. 48 (1992) 2104–2107.

[29] C. De Libdration, T. Cedex, Synthesis, Crystal Structure, and Magnetic Properties of $Co_3(HPO_4)_2,(OH)_2$, Related to the Mineral Lazulite, J. Solid state Chem. 92 (1991) 273–285.

[30] T.M. Masikhwa, F. Barzegar, J.K. Dangbegnon, A. Bello, M.J. Madito, D. Momodu, N. Manyala, Asymmetric supercapacitor based on VS_2 nanosheets and activated carbon materials, RSC Adv. 6 (2016) 38990–39000.

[31] F. Casadio, A. Bezúr, I. Fiedler, K. Muir, T. Trad, S. MacCagnola, Pablo Picasso to Jasper Johns: A Raman study of cobalt-based synthetic inorganic pigments, J. Raman Spectrosc. 43 (2012) 1761–1771.

[32] D. Momodu, A. Bello, J. Dangbegnon, F. Barzeger, M. Fabiane, N. Manyala, P_3HT:PCBM/nickel-aluminum layered double hydroxide-graphene foam composites for supercapacitor electrodes, J. Solid State Electrochem. 19 (2014) 445–452.

[33] C. Xiong, T. Li, T. Zhao, A. Dang, H. Li, X. Ji, W. Jin, S. Jiao, Y. Shang, Y. Zhang, Reduced graphene oxide-carbon nanotube grown on carbon fiber as binder-free electrode for flexible high-performance fiber supercapacitors, Compos. Part B Eng. 116 (2017) 7–15.

[34] J.S. Park, A. Reina, R. Saito, J. Kong, G. Dresselhaus, M.S. Dresselhaus, G′ band Raman spectra of single, double and triple layer graphene, Carbon 47 (2009) 1303–1310.

[35] T.M. Masikhwa, M.J. Madito, D.Y. Momodu, J.K. Dangbegnon, O. Guellati, A. Harat, M. Guerioune, F. Barzegar, N. Manyala, High performance asymmetric supercapacitor based on CoAl-LDH/GF and activated carbon from expanded graphite, RSC Adv. 6 (2016) 46723–46732.

[36] J.W. Lee, T. Ahn, J.H. Kim, J.M. Ko, J.D. Kim, Nanosheets based mesoporous NiO microspherical structures via facile and template-free method for high performance

supercapacitors, Electrochim. Acta. 56 (2011) 4849–4857.

[37] K.O. Oyedotun, M.J. Madito, D.Y. Momodu, A.A. Mirghni, T.M. Masikhwa, N. Manyala, Synthesis of ternary NiCo-MnO_2 nanocomposite and its application as a novel high energy supercapattery device, Chem. Eng. J. 335 (2018) 416–433.

[38] S. Lehtimäki, A. Railanmaa, J. Keskinen, M. Kujala, S. Tuukkanen, D. Lupo, Performance, stability and operation voltage optimization of screen-printed aqueous supercapacitors, Sci. Rep. 7 (2017) 1–9.

[39] B.G. Choi, M. Yang, W.H. Hong, J.W. Choi, Y.S. Huh, 3D macroporous graphene frameworks for supercapacitors with high energy and power densities, ACS Nano. 6 (2012) 4020–4028.

[40] F. Barzegar, A. Bello, D.Y. Momodu, J.K. Dangbegnon, F. Taghizadeh, M.J. Madito, T.M. Masikhwa, N. Manyala, Asymmetric supercapacitor based on an α-MoO_3 cathode and porous activated carbon anode materials, RSC Adv. 5 (2015) 37462–37468.

[41] B. Hu, X. Qin, A.M. Asiri, K.A. Alamry, A.O. Al-Youbi, X. Sun, Synthesis of porous tubular C/MoS_2 nanocomposites and their application as a novel electrode material for supercapacitors with excellent cycling stability, Electrochim. Acta. 100 (2013) 24–28.

[42] A. Balducci, D. Belanger, T. Brousse, J.W. Long, W. Sugimoto, Perspective—A Guideline for Reporting Performance Metrics with Electrochemical Capacitors: From Electrode Materials to Full Devices, J. Electrochem. Soc. 164 (2017) A1487–A1488.

[43] A. Laheäär, P. Przygocki, Q. Abbas, F. Béguin, Appropriate methods for evaluating the efficiency and capacitive behavior of different types of supercapacitors, Electrochemistry Communications 60 (2015) 21–25

[44] D. Momodu, A. Bello, K. Oyedotun, F. Ochai-Ejeh, J. Dangbegnon, M. Madito, N. Manyala, Enhanced electrochemical response of activated carbon nanostructures from tree-bark biomass waste in polymer-gel active electrolytes, RSC Adv. 7 (2017) 37286–37295.

[45] M. Minakshi, D. Mitchell, R. Jones, F. Alenazey, T. Watcharatharapong, S. Chakraborty, R. Ahuja, Shape-Controlled Synthesis of Co_2P Nanostructures and Their Application in Supercapacitors, Nanoscale. 8 (2016) 11291–11305.

[46] S. Wang, H. Pang, S. Zhao, W. Shao, N. Zhang, J. Zhang, J. Chen, S. Li, $NH_4CoPO_4 \cdot H_2O$ microbundles consisting of one-dimensional layered microrods for high performance supercapacitors, RSC Adv. 4 (2014) 340–347.

[47] X.-J. Ma, W.-B. Zhang, L.-B. Kong, Y.-C. Luo, L. Kang, Electrochemical performance in alkaline and neutral electrolytes of a manganese phosphate material possessing a broad potential window, RSC Adv. 6 (2016) 40077–40085.

[48] L. Chen, H. Bai, Z. Huang, L. Li, Mechanism investigation and suppression of self-discharge in active electrolyte enhanced supercapacitors, Energy Environ. Sci. **7 (**2014) 1750-1759